

## **Perovskite Oxynitrides for Plasma-Driven Ammonia Synthesis: Unlocking the Potential of Lattice Nitrogen under Mild Conditions**

Jiayang Li<sup>1</sup>, Zihao Zhang<sup>1</sup>, Chunxiang Yang<sup>2</sup>, Hangjian Zhang<sup>1</sup>, Yuxiang Kong<sup>1</sup>, Ruike Tan<sup>1</sup>, Qingchuan Xiong<sup>1</sup>, Hongyu Jiang<sup>1</sup>, Xiaoyue Mu<sup>2\*</sup> & Lu Li<sup>1,2\*</sup>

### **Affiliation:**

<sup>1</sup>State Key Laboratory of Inorganic Synthesis and Preparative Chemistry, College of Chemistry, Jilin University, Changchun 130012, China

<sup>2</sup>College of Chemistry, Jilin University, Changchun 130012, China

Correspondence to: [xymu@jlu.edu.cn](mailto:xymu@jlu.edu.cn); [luli@jlu.edu.cn](mailto:luli@jlu.edu.cn)

This PDF file includes:

Scheme S1, S2

Figures S1 to S33

Tables S1, S2

## Materials and Methods

### 1. Materials

All commercially available compounds were purchased from Innochem, Sinopharm, and Aladdin company, and used without further purification. The purities of hydrogen, nitrogen, and argon are all 99.995%.

### 2. Characterization.

Powder x-ray diffraction (XRD) analyses were carried out on a Rigaku D/Max 2550 diffractometer using copper K $\alpha$  radiation at 200 mA and 50 kV ( $\lambda = 1.5418$  Å). Transmission electron microscopy (TEM) and high-resolution transmission electron microscopy (HRTEM) images were taken on a Philips-FEITecnaig2S-Twin using a 200 kV field emission gun. Scanning electron microscopy (SEM) analysis was collected using a Helios NanoLab 600I from FEI Company. The Brunauer-Emmett-Teller (BET) surface areas of the samples were measured from the adsorption of N<sub>2</sub> at 77 K by using a Micromeritics ASAP 2020M system. X-ray photoelectron spectroscopy (XPS) was used to evaluate both the chemical composition and oxidation state of the catalyst surfaces. Photoelectron spectra were recorded with a Thermo Scientific ESCALAB 250Xi spectrometer equipped with Al-K $\alpha$  radiation ( $h\nu = 1486.8$  eV). The corresponding binding energies were calibrated with the C 1s line at 284.8 eV as a reference. Simultaneous thermal analysis - mass spectrometry was performed using a NETZSCH STA449F3 QMS403D analyzer. Raman spectra were conducted on a confocal Raman microscope (LabRAM HR Evolution) equipped with a 532 nm laser. Fourier transform infrared spectroscopy (FTIR) spectra were performed using a Bruker spectrometer 66 V/s Fourier transform spectrometer. Electron paramagnetic resonance (EPR) spectra were recorded on a JES-FA 200 EPR spectrometer. The temperature programmed desorption of ammonia (NH<sub>3</sub>-TPD) was performed using an AutoChem 2920 chemisorption analyzer. Electrical signals were sampled by a four-channel digital oscilloscope (Puyuan, DS1102). The discharge power was calculated using the Q-U Lissajous method.

### 3. Plasma catalytic ammonia synthesis tests.

#### 3.1 Calculation of Parameters.

The rate of ammonia synthesis ( $R_{\text{NH}_3}$ ) is defined as the ratio of the number of moles of ammonia to the amount of catalyst and reaction time used in the performance tests. To make the performance comparable, it was assumed that the amount of catalyst in the 'plasma alone' condition was 0.5 g, the same amount of catalyst used in the other tests.

$$R_{\text{NH}_3} = \frac{\text{Number of moles of produced ammonia } (\mu\text{mol})}{\text{The amount of catalyst used (g)} \times \text{reaction time (h)}}$$

The energy efficiency of the plasma-catalytic process was calculated as follows:

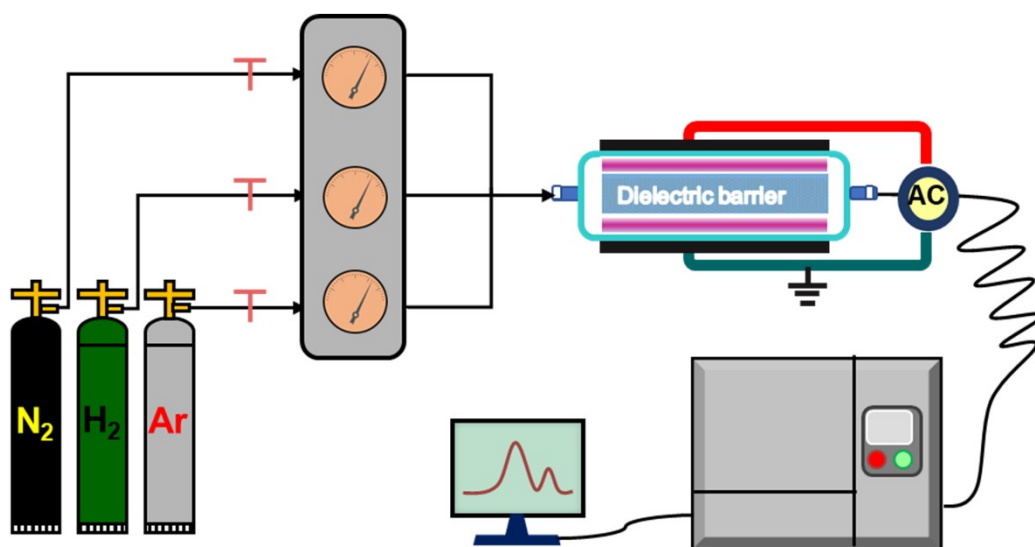
$$\text{Energy Yield} = \frac{M \times C_{\text{out}} \times Q_{\text{after}}}{P_{\text{d}}}$$

where  $M$  is the molar mass of  $\text{NH}_3$ ,  $C_{\text{out}}$  denotes the  $\text{NH}_3$  concentration, and  $Q_{\text{after}}$  is the outlet gas flow rate after the reaction.

### 3.2 $^{15}\text{N}$ isotope-labeling and pulse experiments operation scheme.

The isotope experiments were realized by a closed three-way gas mixing chamber and a plasma reactor in tandem as shown in Scheme S2, where the catalyst was first pretreated by exposure to  $\text{H}_2$  plasma for 10 min, the plasma was then turned off and purged with argon for 30 minutes, switched to  $^{15}\text{N}_2$ . After 10 min, the supply of  $^{15}\text{N}_2$  was stopped and switched quickly to  $\text{H}_2$ , using a mass spectrometer (HAL RC RGA 201) to detect the exit gas and monitor the  $m/z = 2, 17, 18, 29,$  and  $30$  mass changes with time to follow the reaction.

In the pulsed experiments, the plasma was first purged with Ar until all signals were smooth, and then the plasma was turned on to react with a 5%  $\text{H}_2$  - 95% Ar mixture for 30 min, and the plasma was turned off after the decrease in ammonia signal slowed down. After all the signals were smooth, the plasma was purged with argon until the hydrogen signal disappeared, exposed to 10%  $\text{N}_2$  - 95% Ar mixture for 20 min, purged with argon until the nitrogen signal basically disappeared, and then carried out the second cycle, the cycle was carried out three times in total. 5%  $\text{H}_2$  - 95% Ar was replaced with 1%  $\text{CH}_4$  - 99% Ar for a tandem reaction experimental investigation.



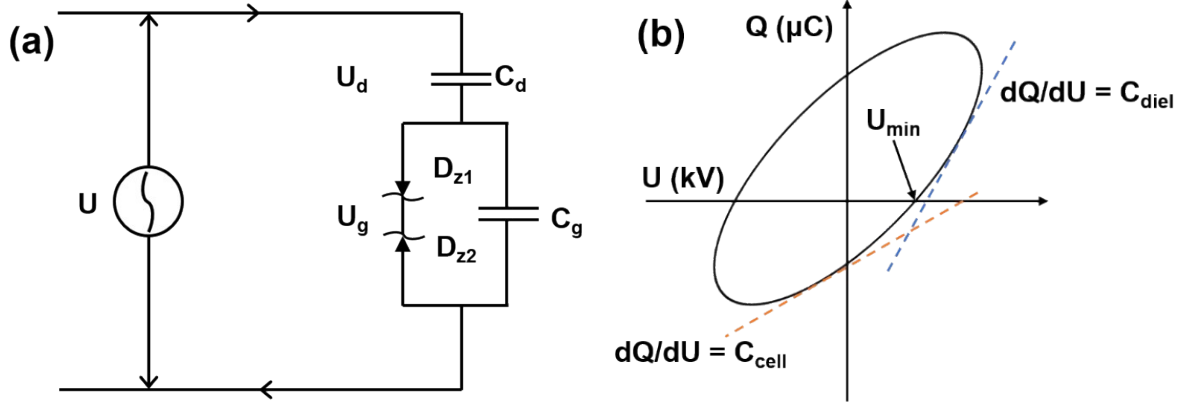
**Scheme S1.** Schematic diagram of isotope-labeling and pulse experiments.

### 3.3 In Situ FTIR Characterization.

For in situ FTIR analysis, an experimental method of exchanging the passage of different gases under heating conditions at 473 K was designed to study the surface nitrogen activation process of LWO and LWON as follows.

Firstly, LWO and LWON were exposed to argon heated to 473 K for 30 min each as background. Next, the catalysts were exposed to a mixture of 75%  $\text{H}_2$  - 25%  $\text{N}_2$  or 5%  $\text{H}_2$  - 95% Ar, and IR spectra were acquired every 2 min.

### 3.4 Discharge parameters.



**Scheme S2.** (a) Equivalent circuit model for a DBD and (b) the corresponding Q-U plots.

$C_g$  (gap capacitance) and  $U_b$  (breakdown voltage) were calculated, based on the DBD equivalent circuit in Scheme S2 and the information from the classical Q-V Lissajous.

The calculation equations are as follows:

$$C_g (\mu\text{F}) = \frac{C_{\text{diel}} (\mu\text{F}) \times C_{\text{cell}} (\mu\text{F})}{C_{\text{diel}} (\mu\text{F}) - C_{\text{cell}} (\mu\text{F})}$$

$$U_b (\text{kV}) = \frac{1}{1 + (C_g (\mu\text{F}) / C_{\text{diel}} (\mu\text{F}))} \times U_{\text{min}} (\text{kV})$$

$$E (\text{kV cm}^{-1}) = \frac{U_b (\text{kV})}{d_{\text{discharge gap}} \times \beta_{\text{volume fraction}}}$$

where  $U_{\text{min}}$  is the minimum external voltage at which plasma ignition occurs and can be determined from the Lissajous figure. The volume fraction factor  $\beta_{\text{volume fraction}}$  calculated by the drainage method is 0.6 and 0.5 for quartz sand filling or quartz sand with catalyst, respectively.<sup>[1-3]</sup>

### 3.5 Calculation of electron density.

The mean electron density ( $n_e$ ) can be determined by:<sup>[4, 5]</sup>

$$n_e (\text{m}^{-3}) = \frac{J (\text{A m}^{-2})}{E (\text{Td}) \times \mu_e \times e}$$

where  $J$  is the current density, defined as the ratio of the average peak discharge current over 3 cycles to the surface area of the one micro-discharge ( $1.05 \times 10^{-6} \text{ m}^2$ ).  $E$  is the electric field, and  $\mu_e$  is the electron mobility calculated from BOLSIG+.  $e$  is the electron charge ( $1.6 \times 10^{-19} \text{ C}$ ).

## 4. Density functional theory (DFT) calculations.

All theoretical calculations were performed by Density Functional Theory (DFT) and run under the Vienna Ab initio Simulation Package (VASP)<sup>[6, 7]</sup>. We used the general gradient approximation (GGA) of PBE.<sup>[8]</sup> to characterize the ion-electron interaction with an all-electron projected parametric wave (PAW)

pseudopotential.<sup>[9]</sup> The cutoff energy was set to 500 eV. For structural relaxation, the convergence criteria for energy and force were  $1 \times 10^{-4}$  eV and  $0.01 \text{ eV}\text{\AA}^{-1}$ , respectively. Based on a  $1 \times 1 \times 1$  LaW(O, N)<sub>3</sub> singlet containing 20 atoms was constructed for LaWO<sub>3</sub> and LaWO<sub>2</sub>N. We calculated the electronic structures of LaWO<sub>3</sub> and LaWO<sub>2</sub>N using the GGA + U method. In this work, we used the method described by Dudarev et al,<sup>[10]</sup> where there is only one valid Hubbard parameter  $U_{\text{eff}} = U - J$  into the Hamiltonian, and we took the value of  $U_{\text{eff}}$  for LaWO<sub>3</sub> and LaWO<sub>2</sub>N to be 5 eV. For the bulk we chose  $4 \times 4 \times 3$  Monkhorst-Pack k-point lattices, and for the (112) surface we chose  $3 \times 2 \times 1$  for energy calculations. Grimme's DFT-D3 method was used to describe van der Waals interactions<sup>[11]</sup> to obtain a better description of the interactions between molecules. Atomic charges were calculated based on the atomic scheme in molecules proposed by Bader.<sup>[12]</sup> The nature of bonding between surfaces and adsorbed molecules was revealed using projected crystal orbital Hamiltonian populations.<sup>[13–S16]</sup>

The  $E_{\text{O}_v}$  and  $E_{\text{N}_v}$  value was the oxygen vacancy formation energy defined by:

$$E_{\text{O}_v} = E_{\text{sub}} + \frac{1}{2}E_{\text{O}_2} - E_{\text{sub} + \text{O atm}}$$

$$E_{\text{N}_v} = E_{\text{sub}} + \frac{1}{2}E_{\text{N}_2} - E_{\text{sub} + \text{N atm}}$$

where  $E_{\text{Sub}}$ ,  $E_{\text{O}_2}$ ,  $E_{\text{N}_2}$ ,  $E_{\text{sub}+\text{O atom}}$ , and  $E_{\text{sub}+\text{N atom}}$  represent the energies of a clean substrate with oxygen vacancy, free oxygen, and a clean substrate, respectively.

The adsorption energy of reaction intermediates was defined as:

$$E_{\text{ads}} = E_{\text{M} + \text{sub}} - E_{\text{sub}} - E_{\text{M}}$$

where  $E_{\text{M-Sub}}$ ,  $E_{\text{Sub}}$ , and  $E_{\text{M}}$  represent the energies of an adsorbed system, a clean substrate, and an adsorbate, respectively.

The  $\Delta G$  value was obtained via the formula:

$$\Delta G = \Delta E + \Delta ZPE - T \times \Delta S$$

where  $\Delta E$  is the reaction energy difference between the product and the reactant occurring on catalysts.  $\Delta ZPE$  and  $\Delta S$  are the changes in zero-point energies and entropy at 323.15 K, which were calculated by considering only the vibrational frequencies.

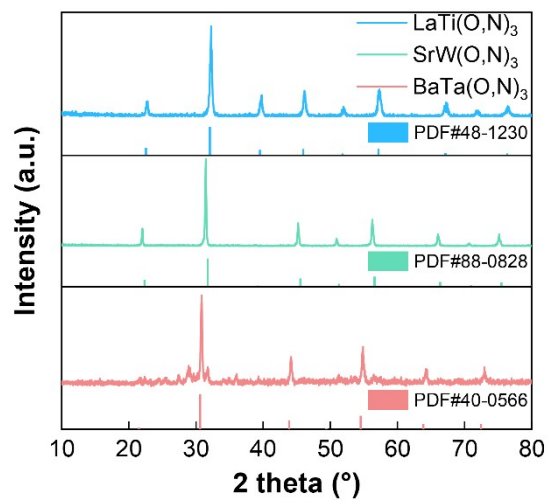


**Figure S1.** XRD patterns of LaTi(O, N)<sub>3</sub>, SrW(O, N)<sub>3</sub>, and BaTa(O, N)<sub>3</sub> with the standard patterns (PDF # 48-1230, 88-0828, and 40-0566).

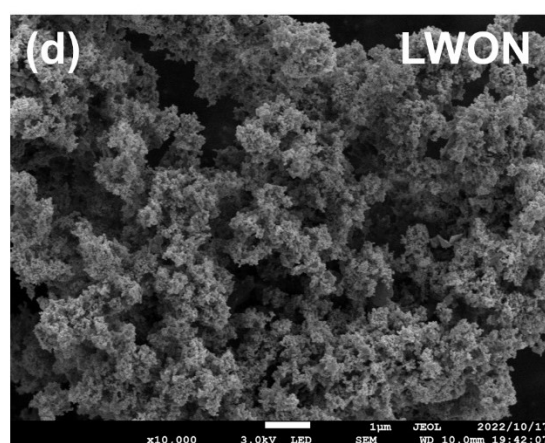
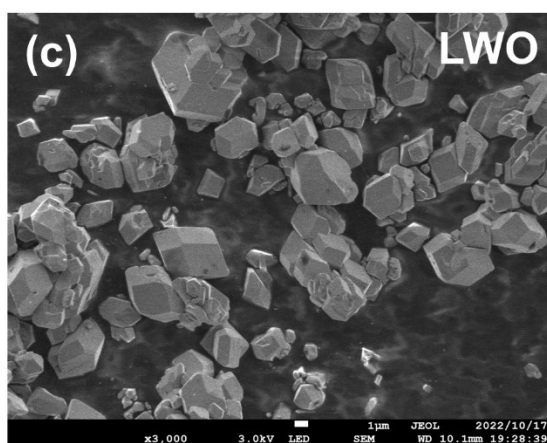
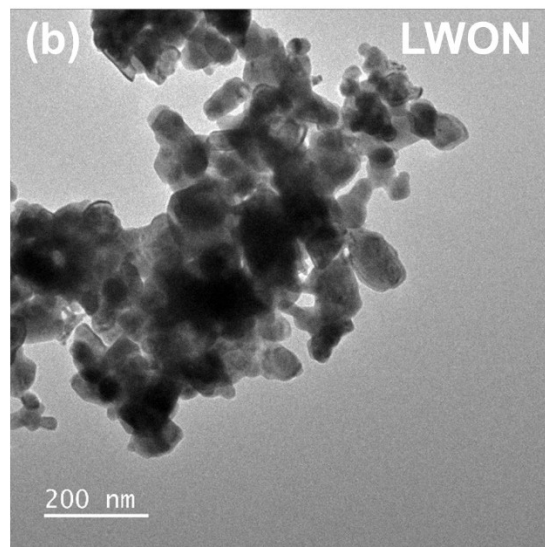
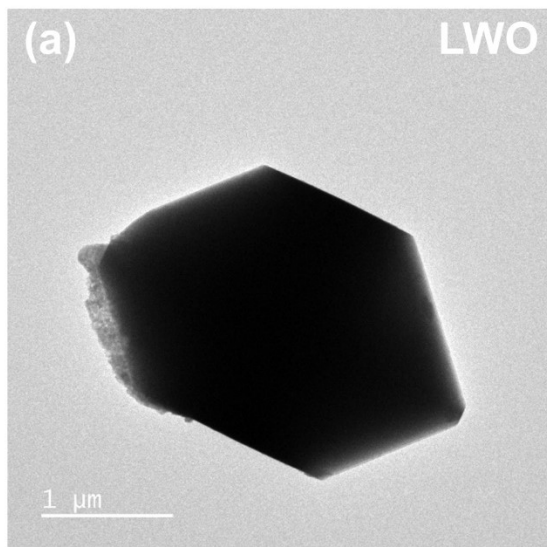


**Figure S2.** TEM and SEM images of LWO (a), (c) and LWON (b), (d).

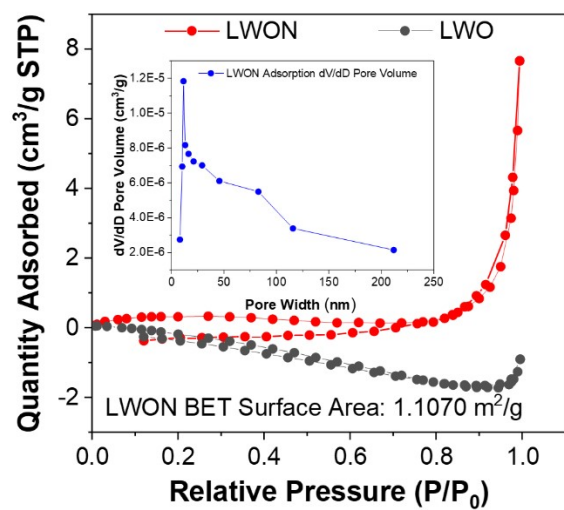


**Figure S3.** Nitrogen adsorption-desorption isotherms BJH pore-size distribution curves of LWO and LWON.

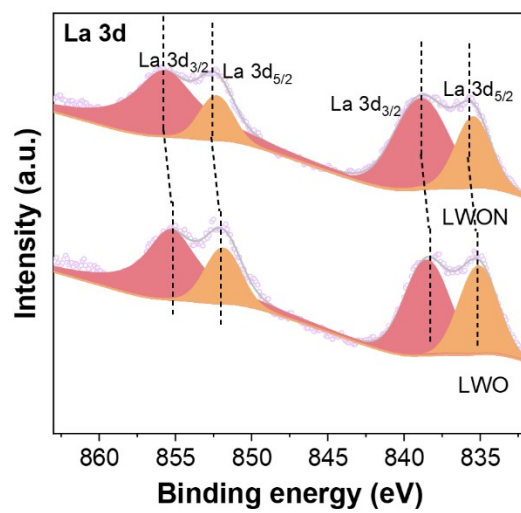


**Figure S4.** XPS spectra of La 3d for LWO and LWON.

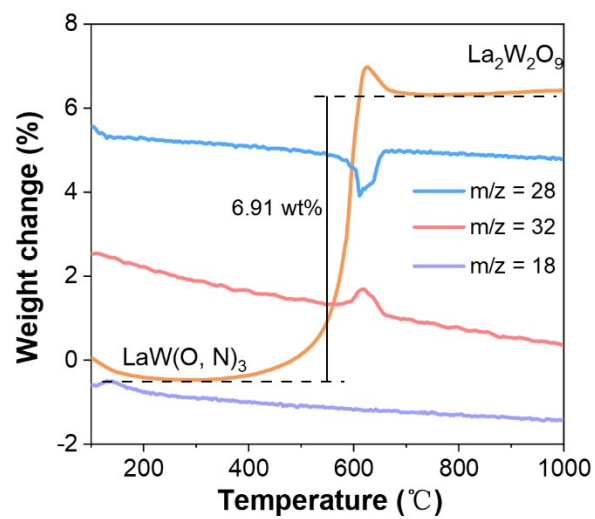


**Figure S5.** TGA-MS curves of LWON. Heating and cooling rates are 10 K/min. The weight gain is attributed to the oxidation of  $\text{LaW(O, N)}_3$  to  $\text{La}_2\text{W}_2\text{O}_9$ .

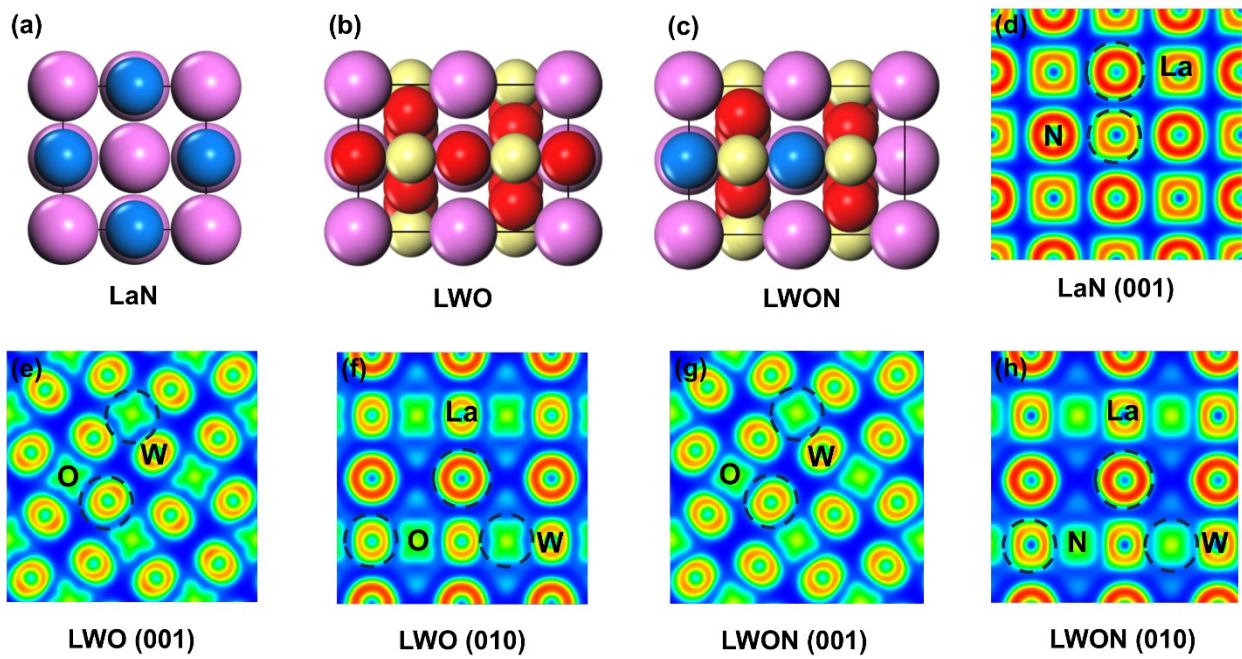


**Figure S6.** Optimized structures of LaN (a), LWO (b), and LWON (c). Electronic location functions (ELF) of LaN (d), LWO (e), (f), and LWON (g), (h).

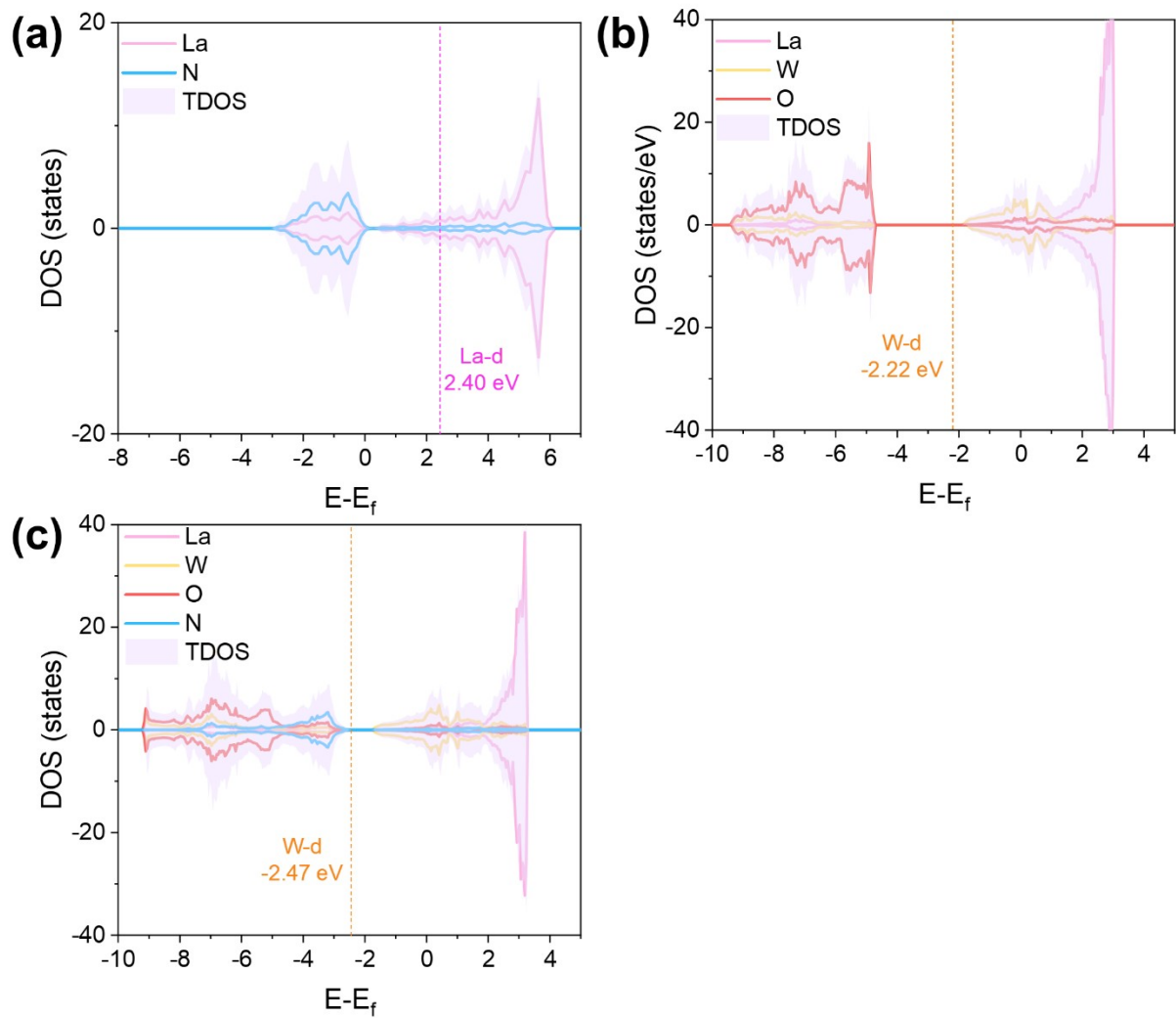


**Figure S7.** Density of states (DOS) of LaN (a), LWO (b), and LWON (c).

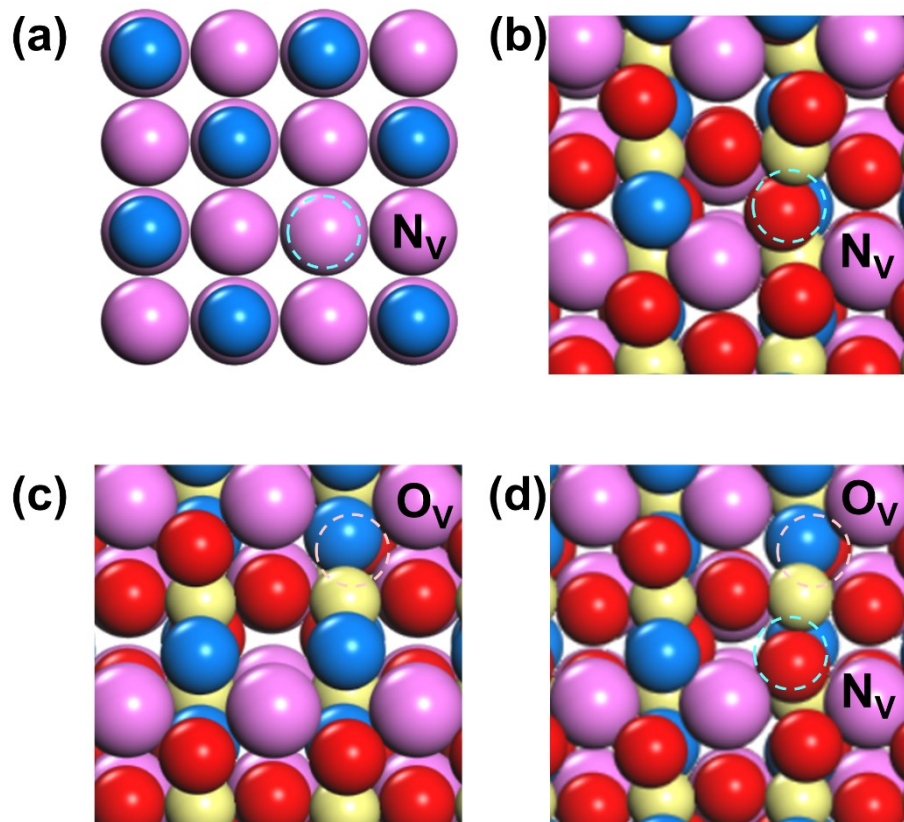


**Figure S8.** Possible sites of O and N vacancies in LaN (a), LWO (b), and LWON (c), (d).

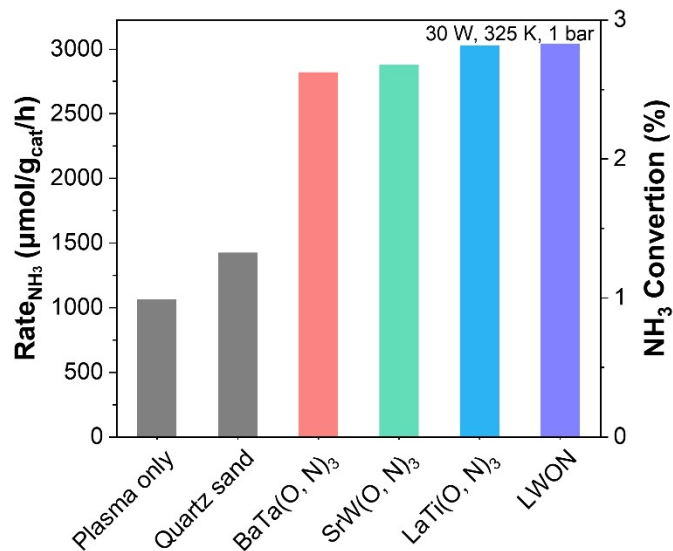


**Figure S9.** Rate<sub>NH<sub>3</sub></sub> and NH<sub>3</sub> Conversion of plasma only and plasma-catalytic systems (with Quartz sand, LaTi(O, N)<sub>3</sub>, LaTi(O, N)<sub>3</sub>, BaTa(O, N)<sub>3</sub>, and LaW(O, N)<sub>3</sub>, P<sub>d</sub> = 30 W, Q<sub>gas</sub> = 40 ml/min, N<sub>2</sub>:H<sub>2</sub> = 1:3, at 323 K and 1 bar)

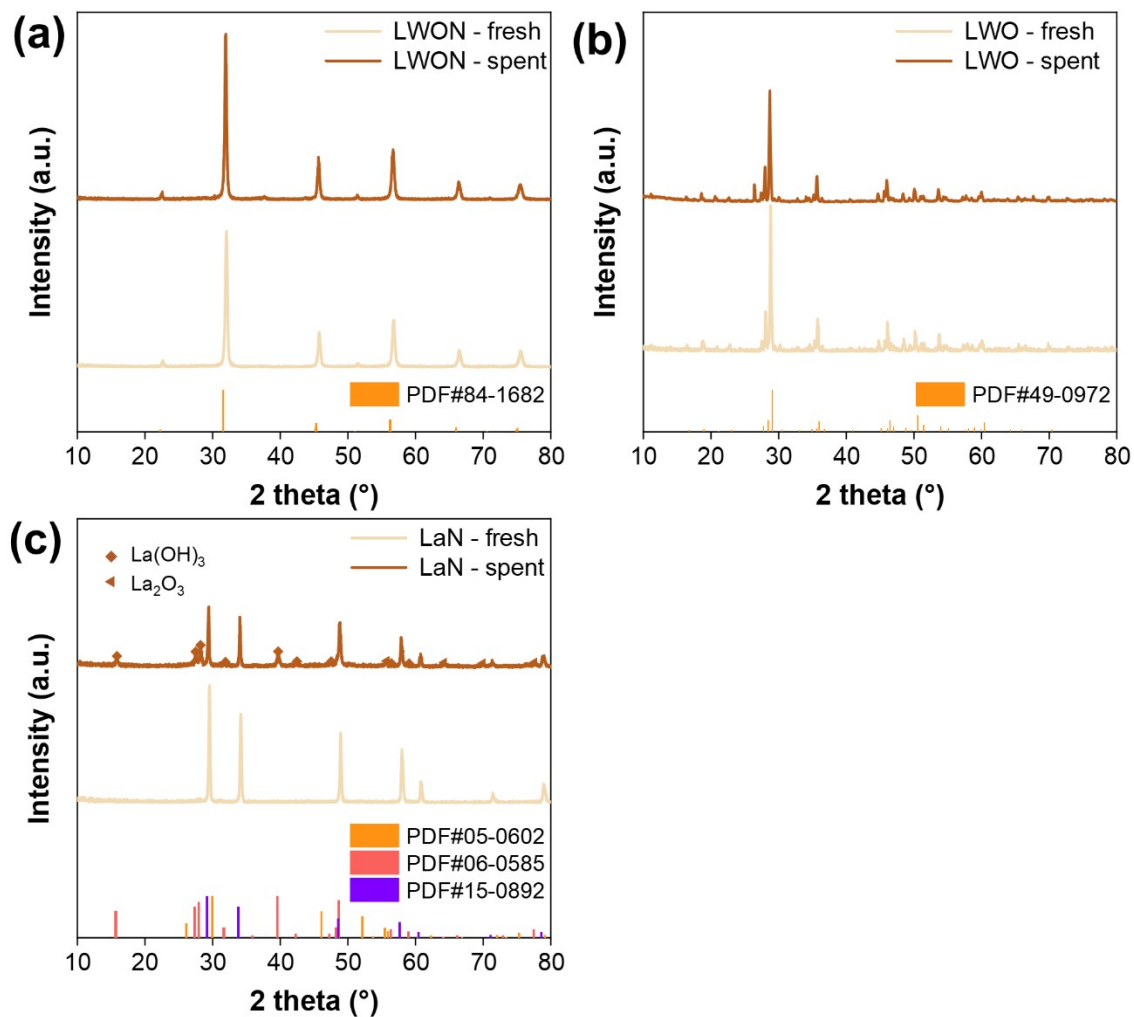


**Figure S10.** XRD patterns of the fresh and the spent catalysts after plasma-catalytic NH<sub>3</sub> synthesis for LWON (a), LWO (b), and LaN (c). (JCPDF no. 84-1682, 49-0972, 05-0602, 06-0585, 15-0892)

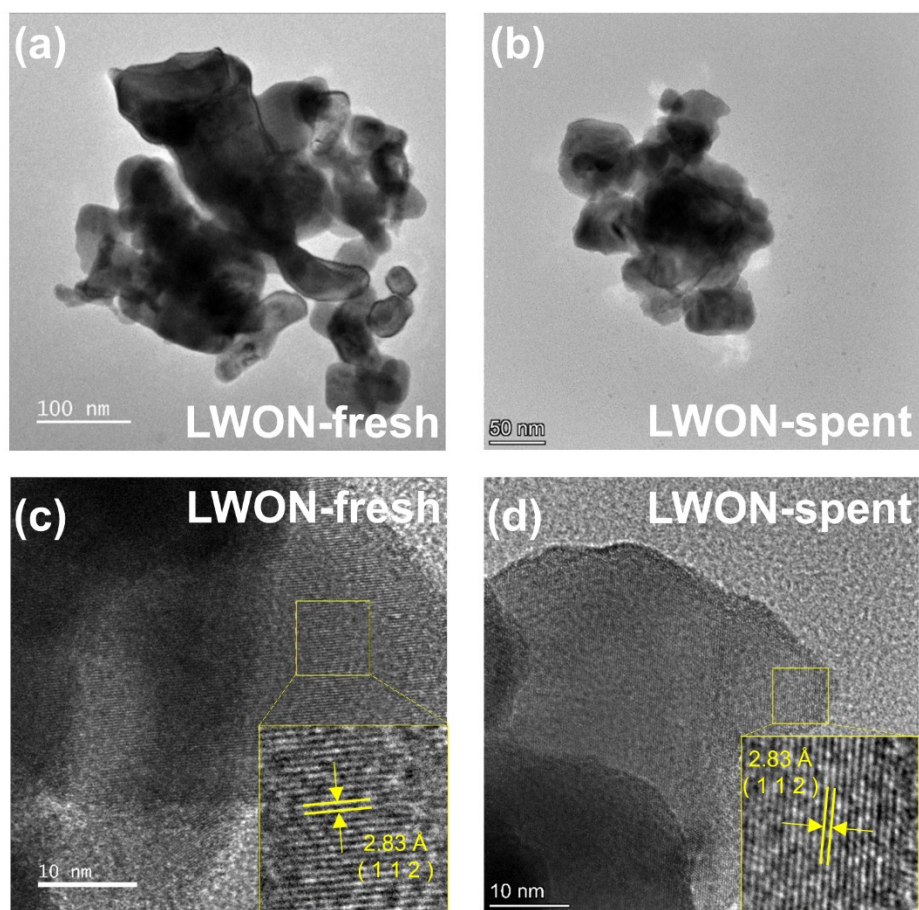


**Figure S11.** HRTEM images of the fresh and spent catalysts after 160 h plasma-catalytic  $\text{NH}_3$  synthesis for LWON.

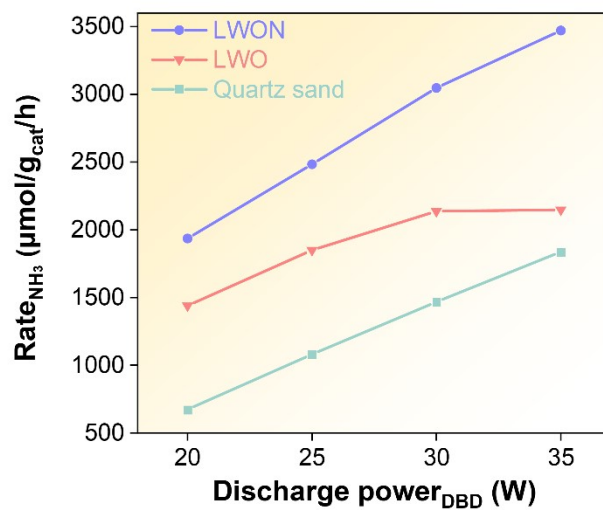


**Figure S12.** Effect of plasma-catalytic systems (with Quartz sand, LWO, and LWON) on Rate<sub>NH<sub>3</sub></sub> of ammonia at different discharge powers. ( $Q_{\text{gas}} = 40$  ml/min,  $N_2:H_2 = 1:3$ , Discharge power: 20–35 W, at 323 K and 1 bar)..

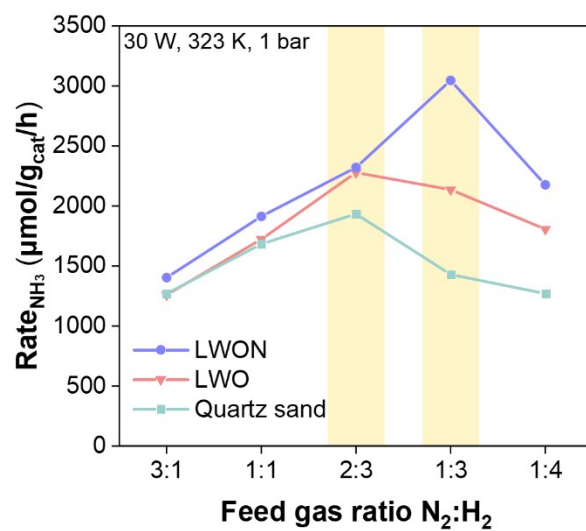


**Figure S13.** Effect of plasma-catalytic systems (with Quartz sand, LWO, and LWON) on  $\text{Rate}_{\text{NH}_3}$  for different feed gas ratios. ( $Q_{\text{gas}} = 40 \text{ ml/min}$ , Discharge power = 30 W, at 323 K and 1 bar)

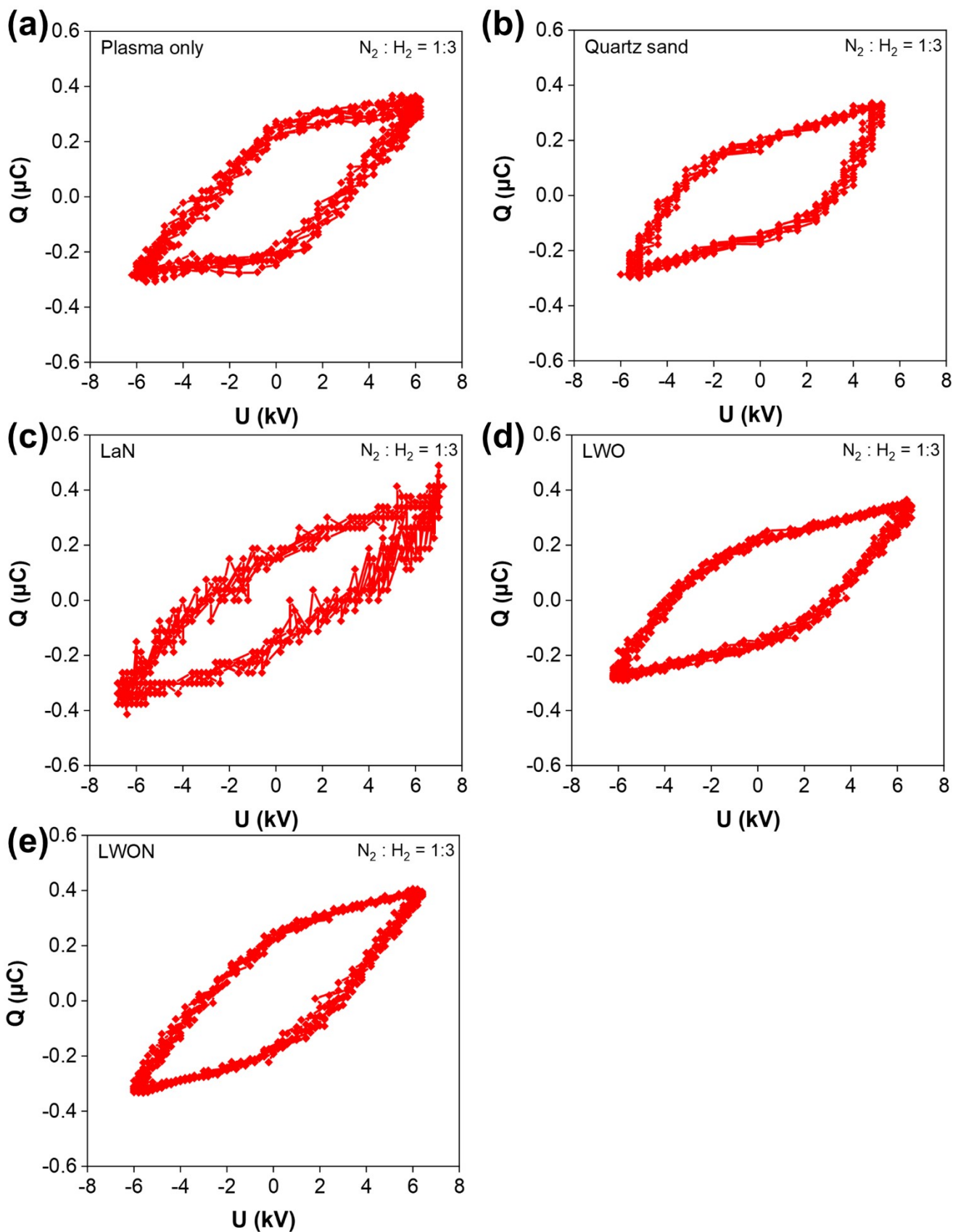


**Figure S14.** Lissajous figures of plasma only (a), packed with Quartz sand (b), LaN (c), LWO (d), LWON (e).

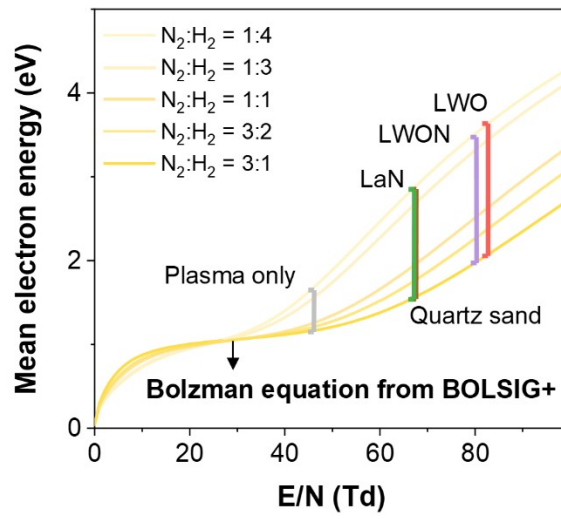


**Figure S15.** Calculated mean electron energy for plasma only, quartz sand, LaN, LWO, and LWON.

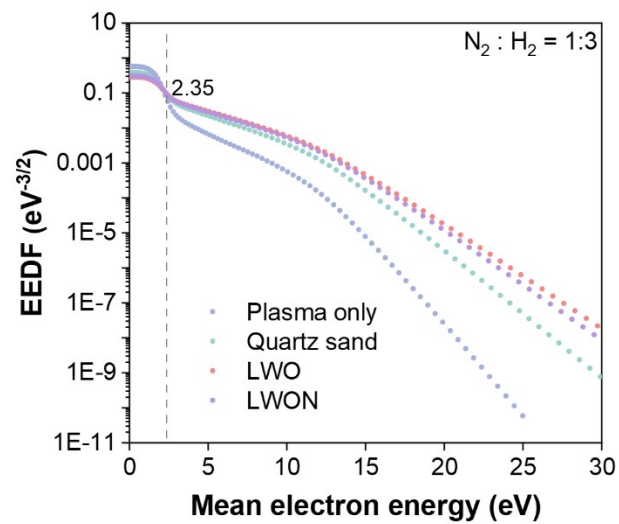


**Figure S16.** Calculated EEDF for plasma only, packed Quartz sand, LWO, and LWON.

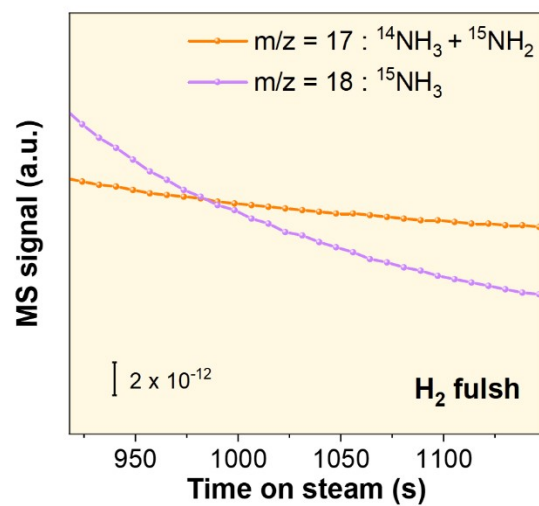


**Figure S17.** Localized enlargement of the reaction time profiles for  $\text{NH}_3$  synthesis from  $^{15}\text{N}_2$  over fresh LWON.

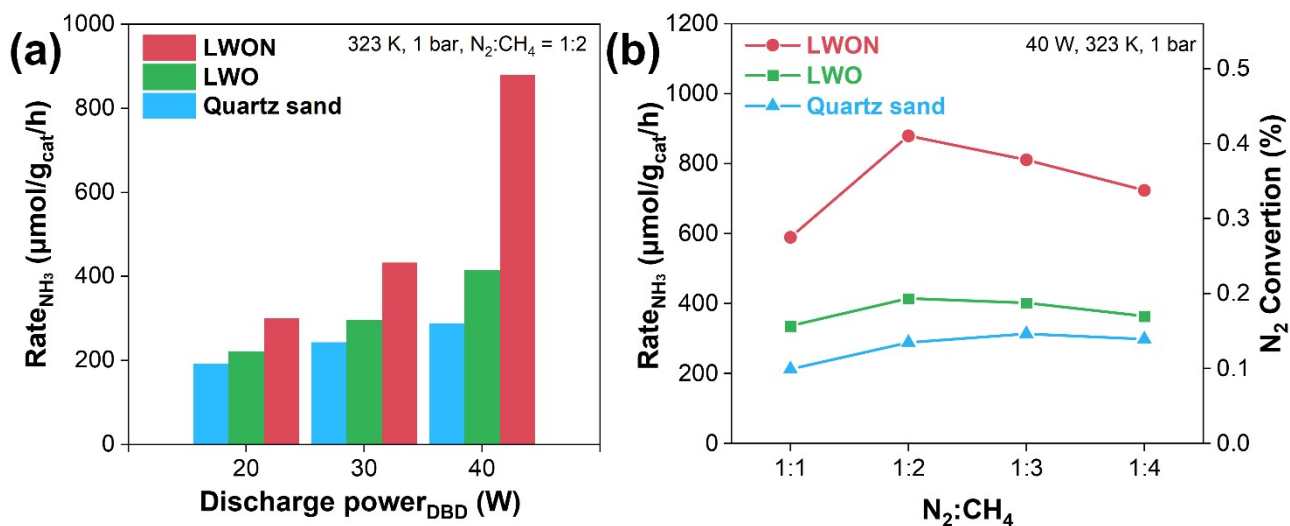


**Figure S18.** (a) Effect of plasma-catalytic systems (with Quartz sand, LWO, and LWON) on  $\text{Rate}_{\text{NH}_3}$  of ammonia at different discharge powers. ( $Q_{\text{gas}} = 60 \text{ ml/min}$ ,  $N_2:CH_4 = 1:2$ , Discharge power: 20–40 W, at 323 K and 1 bar). (b) Effect of plasma-catalytic systems (with Quartz sand, LWO, and LWON) on  $\text{Rate}_{\text{NH}_3}$  for different  $N_2:CH_4$  feed gas ratios. (Discharge power = 40 W, at 323 K and 1 bar).

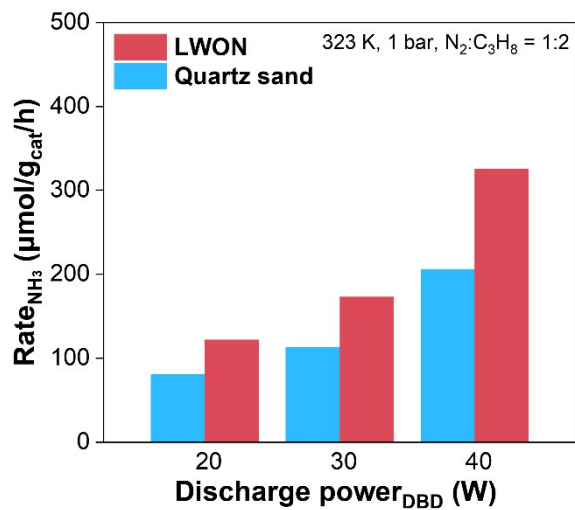


**Figure S19.** (a) Effect of plasma-catalytic systems (with Quartz sand, LWO, and LWON) on Rate<sub>NH<sub>3</sub></sub> of ammonia at different discharge powers. (Q<sub>gas</sub> = 60 ml/min, N<sub>2</sub>:C<sub>3</sub>H<sub>8</sub> = 1:2, Discharge power: 20–40 W, at 323 K and 1 bar).

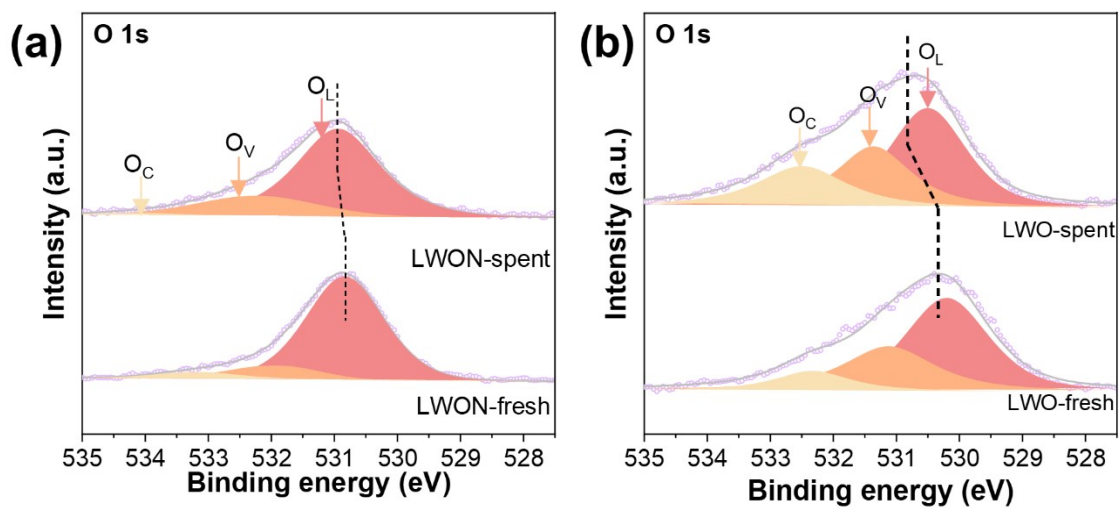


**Figure S20.** XPS spectra of O 1s for LWON (a) and LWO (b) after plasma-catalytic NH<sub>3</sub> synthesis.

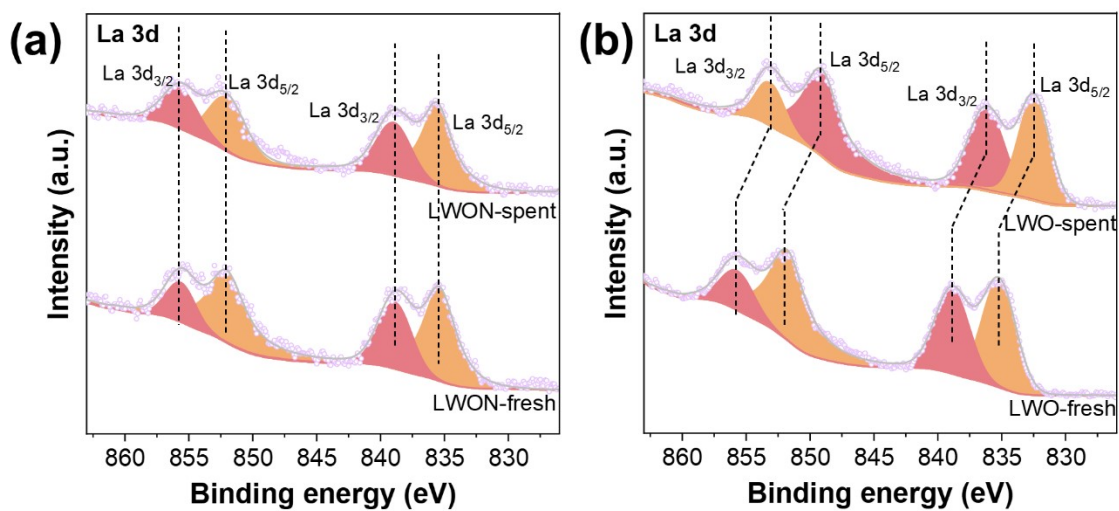


**Figure S21.** XPS spectra of La 3d for LWON (a) and LWO (b) after plasma-catalytic NH<sub>3</sub> synthesis.

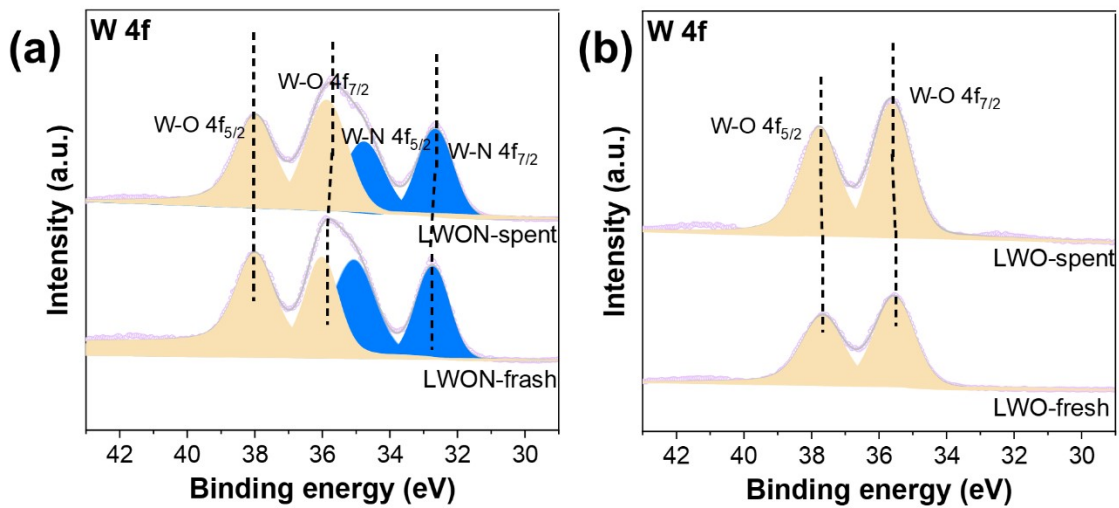


**Figure S22.** XPS spectra of W 4f for LWON (a) and LWO (b) after plasma-catalytic NH<sub>3</sub> synthesis.

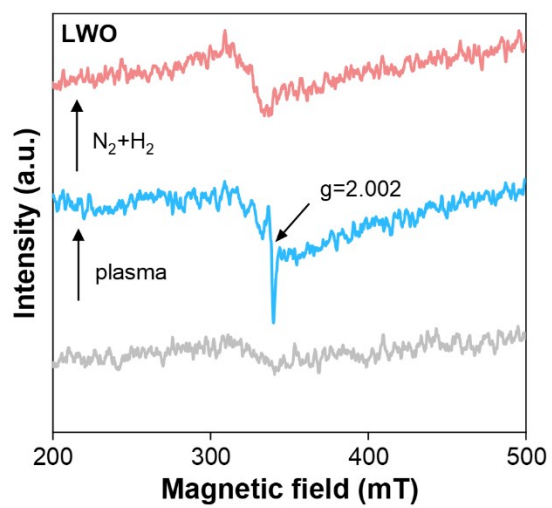


**Figure S23.** Room-temperature X-band EPR spectra of LWO before and after exposure to a mixture of N<sub>2</sub> and H<sub>2</sub> under plasma treatment.

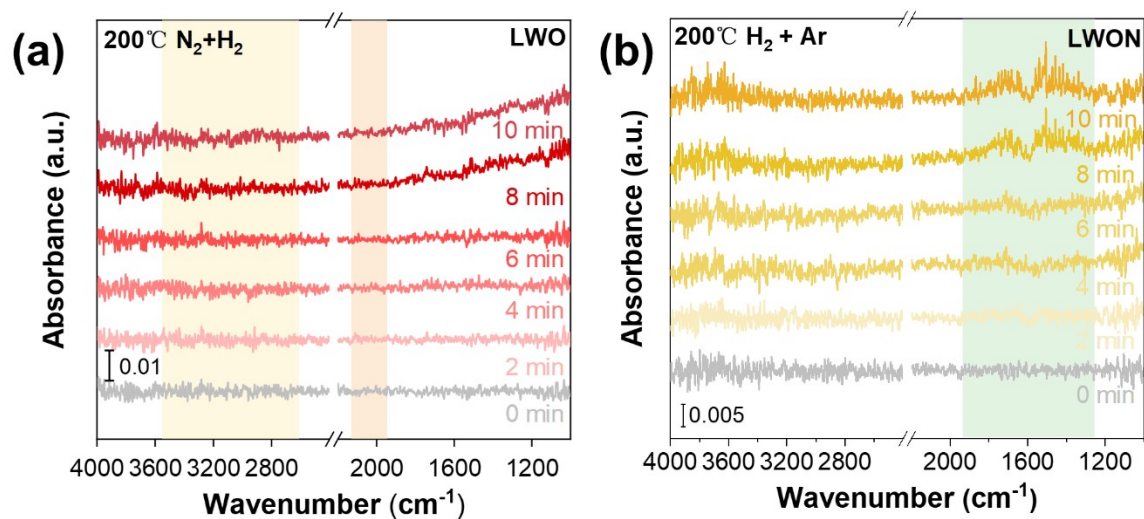


**Figure S24.** In-situ FTIR spectra of LWO (a) and LWON (b) recorded at 473 K when exposed to a mixture of 25%N<sub>2</sub> and 75%H<sub>2</sub> or 5%H<sub>2</sub>-95%Ar.

The peaks between 1252-1927 cm<sup>-1</sup> are attributed to the deformation vibration peaks of NH species.

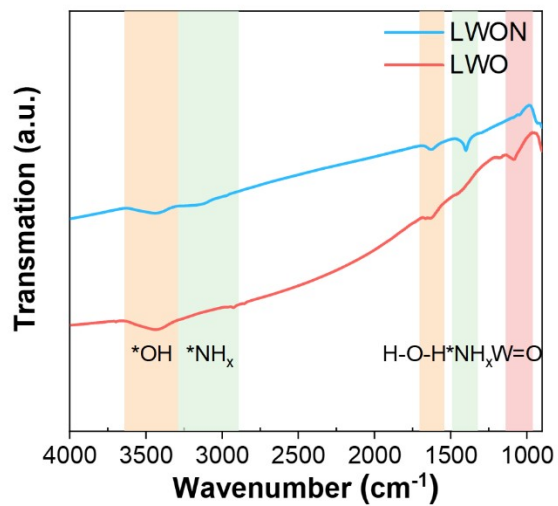


**Figure S25.** FT-IR spectra of LWON and LWO after plasma-catalytic NH<sub>3</sub> synthesis.

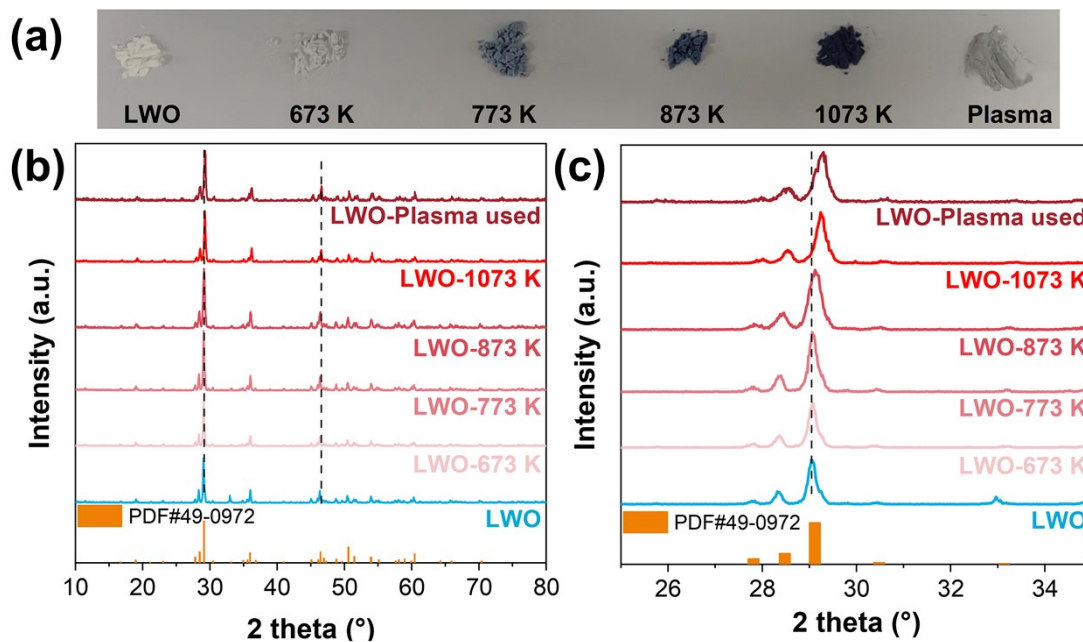


**Figure S26.** Image and XRD patterns of LWO before(fresh) and after heating in 5% $H_2$ -95%Ar at various temperatures or plasma treating. (JCPDF no. 49-0972)

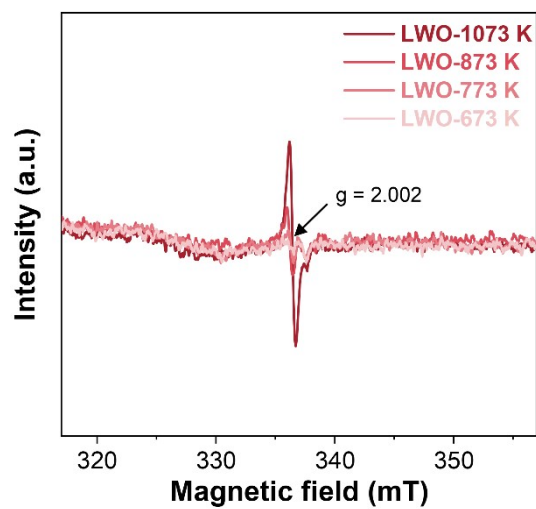


**Figure S27.** Room-temperature X-band EPR spectra of LWO after heating in 5% $H_2$ -95%Ar at various temperatures.

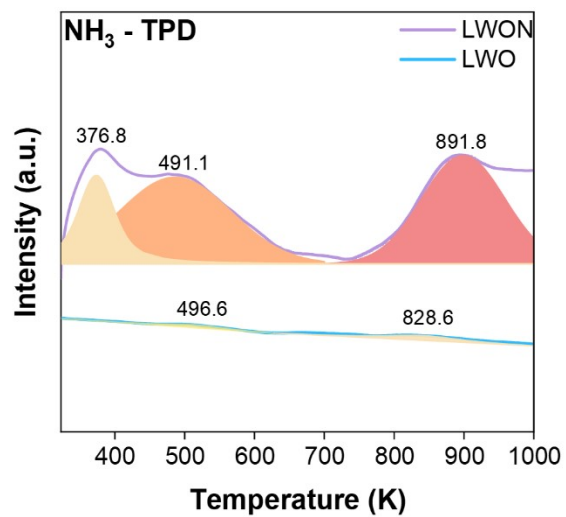


**Figure S28.** The NH<sub>3</sub>-TPD profiles of LWO and LWON.

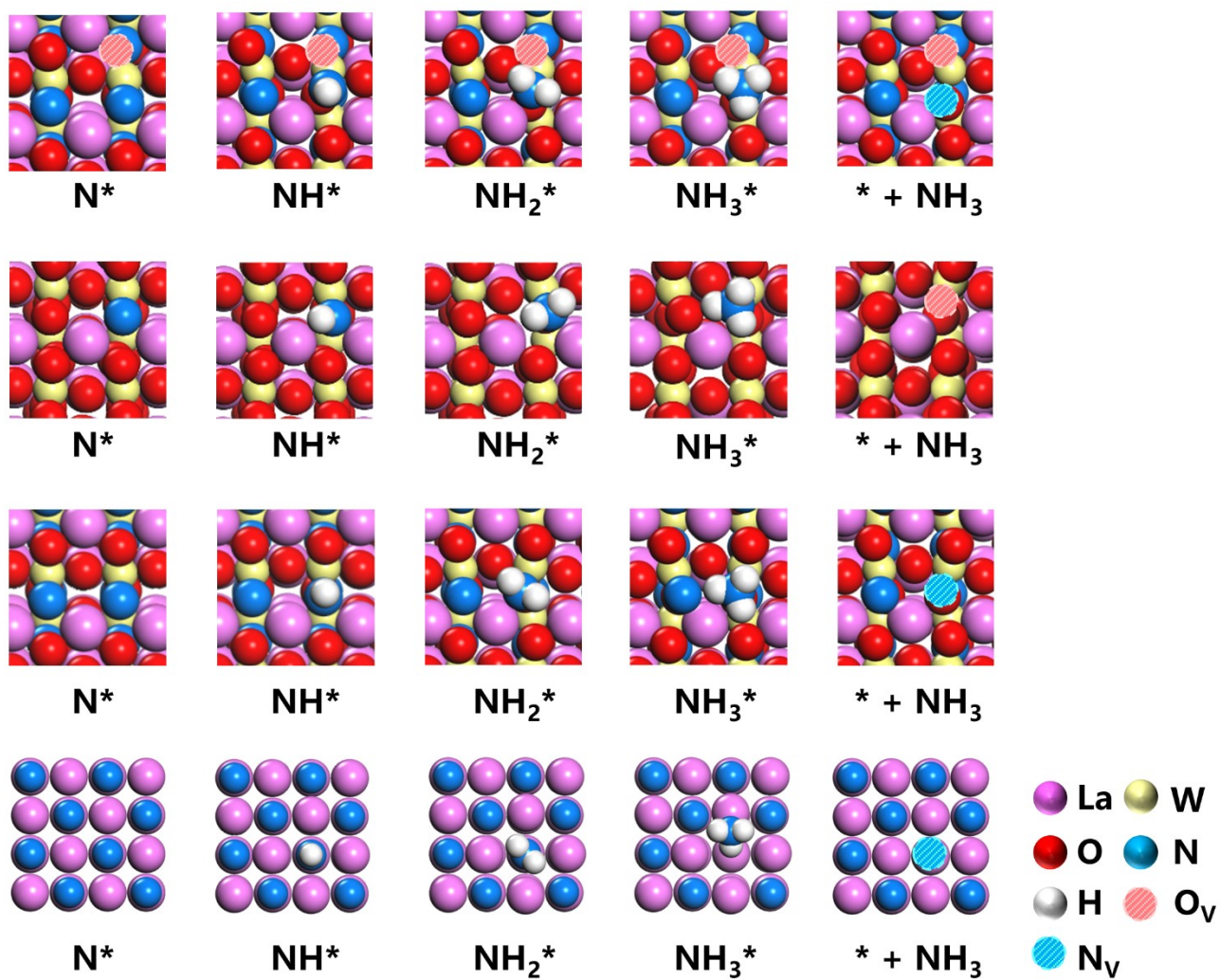


**Figure S29.** Optimized structures for the N hydrogenation reaction on LaN, LWO, and LWON. (top view)

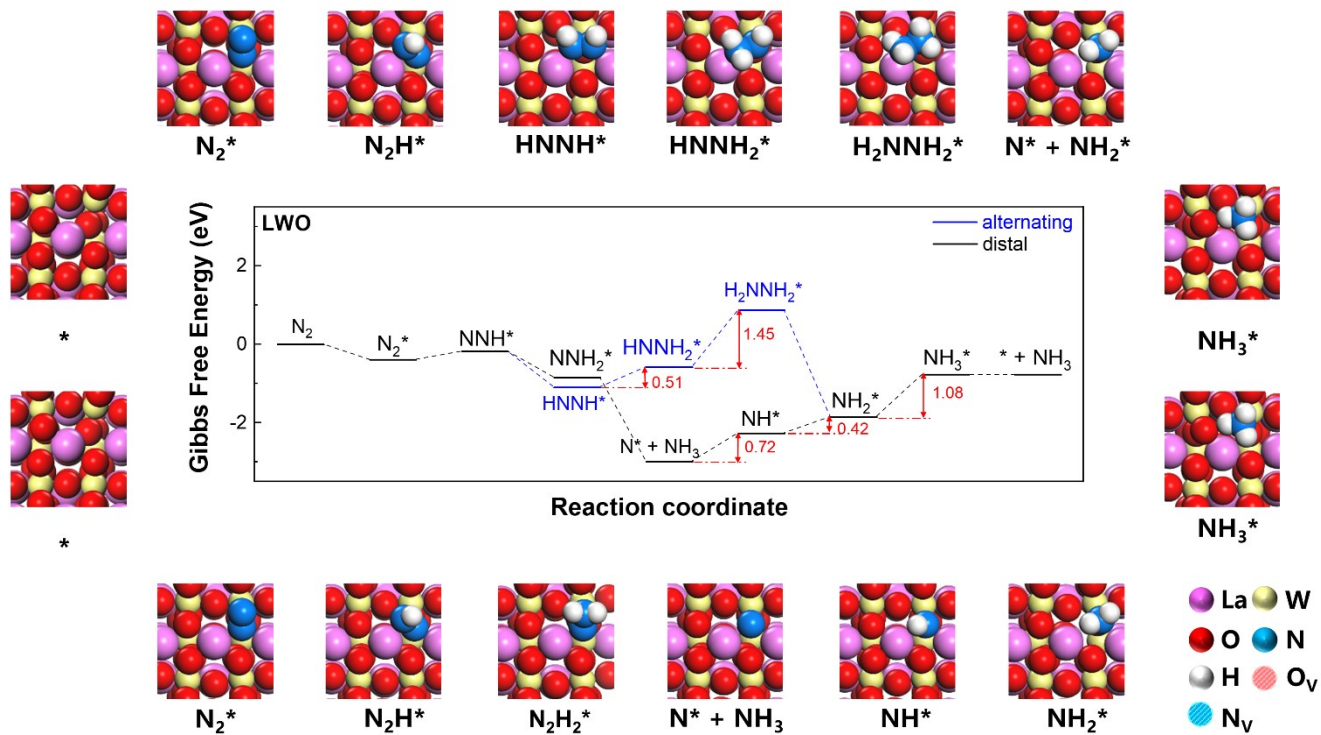


**Figure S30.** Free energy diagram and optimized structures for the  $N_2$  hydrogenation reaction on LWO. (top view)

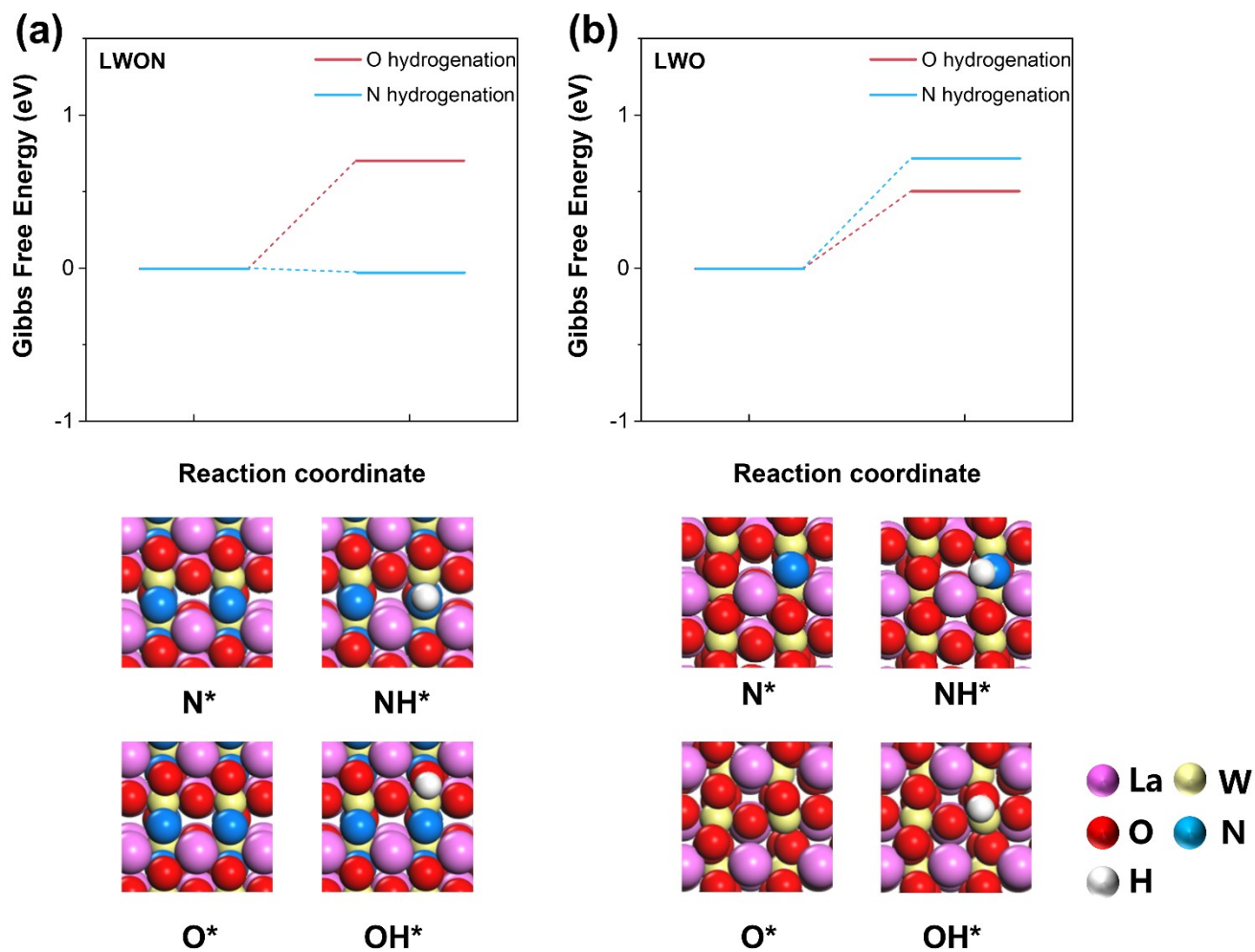


**Figure S31.** Free energy diagram and optimized structures for the O hydrogenation and N hydrogenation process on LWO and LWON. (top view)

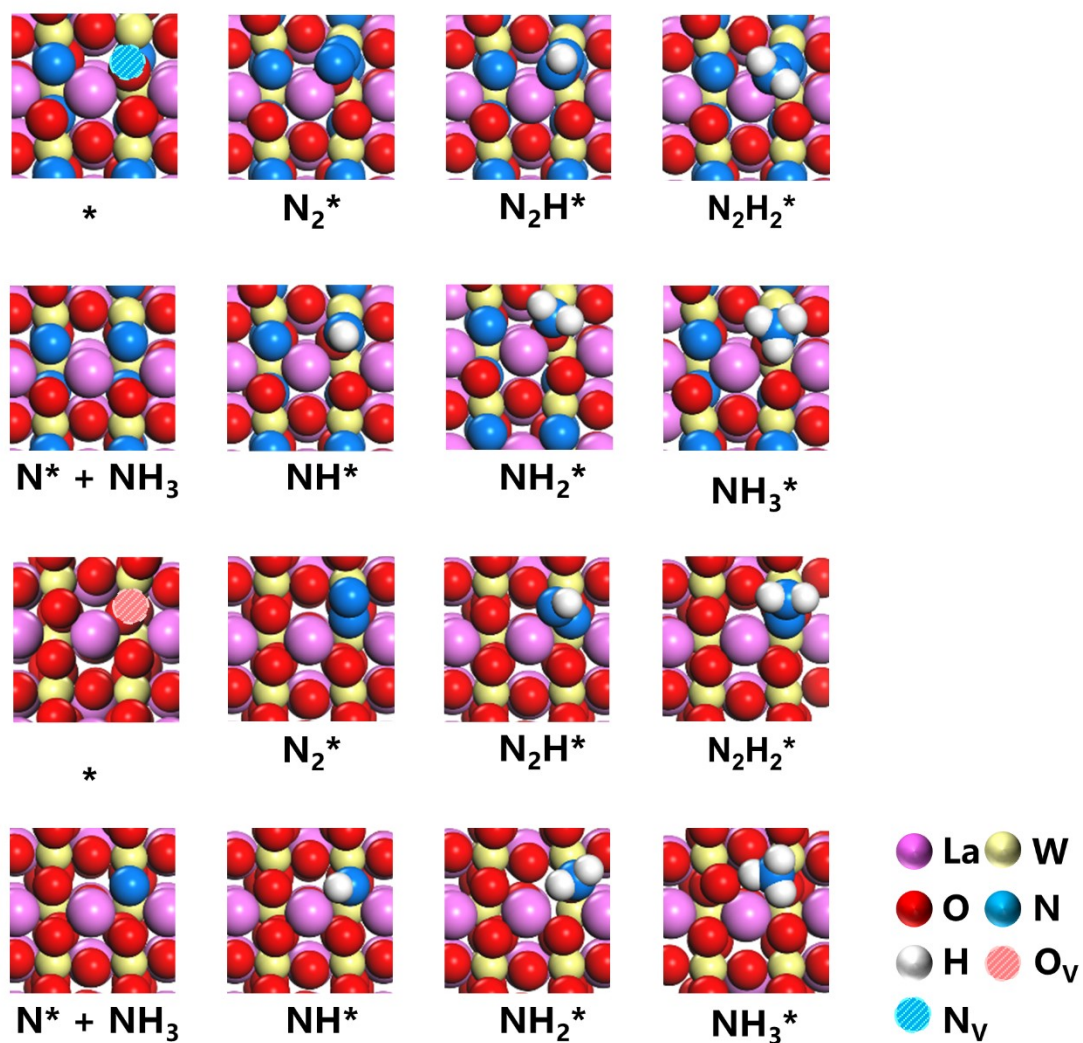


**Figure S32.** Optimized structures for the nitrogen distal hydrogenation process on LWO and LWON. (top view)

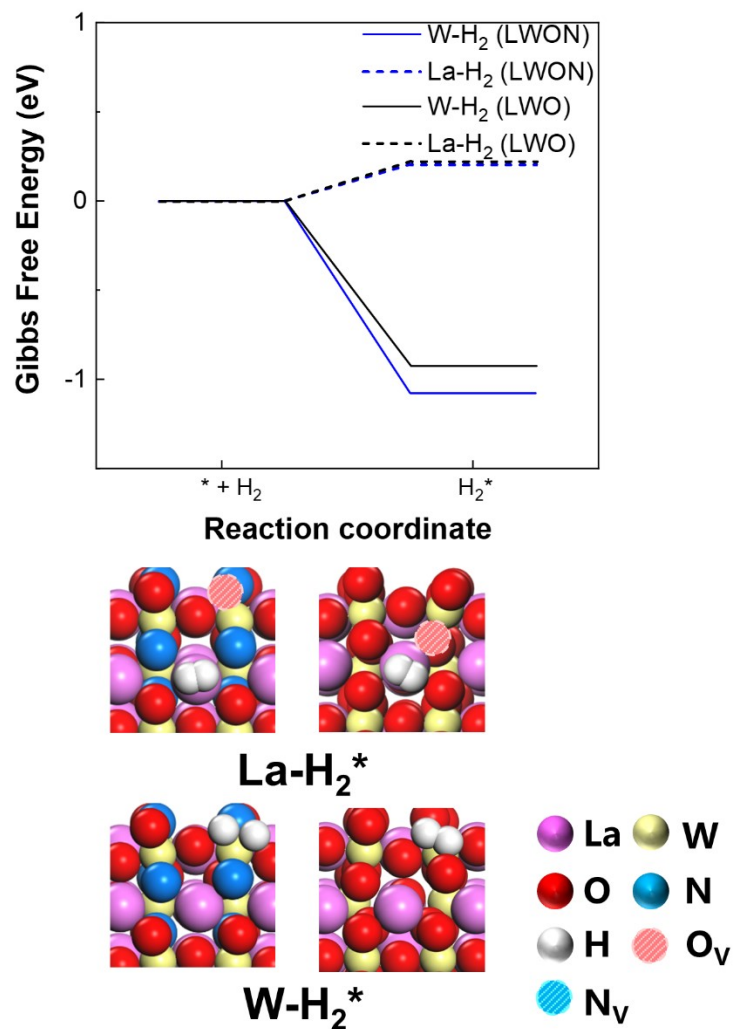


**Figure S33.** Free energy diagram and optimized structures for the hydrogen adsorption process on LWO and LWON. (top view)

**Table S1.** The vacancy formation energies of different O sites.

Position	Vacancy formation energy (eV)
LWON-O <sub>V</sub>	5.590
LWON-N <sub>V</sub>	1.554
LWON(O <sub>V</sub> )-N <sub>V</sub>	1.089
LaN-N <sub>V</sub>	1.634

**Table S2.** Calculated mean electron density for plasma packed with Quartz sand, LaN, LWO, and LWON.

	E(kV·cm <sup>-1</sup> )	E/N(Td)	n <sub>e</sub> (m <sup>-3</sup> )
Quartz sand	15.1 ± 0.2	66.9 ± 0.7	1.26 ± 0.01 × 10 <sup>19</sup>
LaN	15.0 ± 0.3	66.5 ± 1.4	1.27 ± 0.02 × 10 <sup>19</sup>
LWO	18.6 ± 0.1	82.3 ± 0.4	1.51 ± 0.02 × 10 <sup>19</sup>
LWON	17.6 ± 0.1	77.9 ± 0.5	1.60 ± 0.03 × 10 <sup>19</sup>

## References

- [1] U. Kogelschatz, *Plasma Chem. Plasma Process.*, 2003, **23**, 1–46.
- [2] H.-E. Wagner, R. Brandenburg, K. V. Kozlov, A. Sonnenfeld, P. Michel and J. F. Behnke, *Vacuum*, 2003, **71**, 417–436.
- [3] Y. Wang, M. Craven, X. Yu, J. Ding, P. Bryant, J. Huang and X. Tu, *ACS Catal.*, 2019, **9**, 10780–10793.
- [4] M. Ramakers, I. Michielsens, R. Aerts, V. Meynen and A. Bogaerts, *Plasma Processes Polym.*, 2015, **12**, 755–763.
- [5] A. Rahmani and M. Nikravech, *Plasma Chem. Plasma Process.*, 2018, **38**, 517–534.
- [6] G. Kresse and J. Furthmüller, *Comput. Mater. Sci.*, 1999, **6**, 96000080.
- [7] G. Kresse and J. Furthmüller, *Phys. Rev. B*, 1996, **54**, 11169.
- [8] A. V. Krukau, O. A. Vydrov, A. F. Izmaylov, G. E. Scuseria, *J. Chem. Phys.* **2006**, *125*, 224106.
- [9] P. E. Blöchl, *Phys. Rev. B*, 1994, **50**, 17953–17979.
- [10] V. N. Antonov, B. N. Harmon, A. N. Yaresko and A. Ya. Perlov, *Phys. Rev. B*, 1999, **59**, 14571–14582.
- [11] L. A. Burns, Á. V.-Mayagoitia, B. G. Sumpter and C. D. Sherrill, *J. Chem. Phys.*, 2011, **134**, 84107.
- [12] W. Tang, E. Sanville and G. Henkelman, *J. Phys., Condens. Matter: Inst. Phys. J.*, 2009, **21**, 84204.
- [13] R. Dronskowski and P. E. Blochl, *J. Phys. Chem.*, 1993, **97**, 8617–8624.
- [14] V. L. Deringer, A. L. Tchougréeff and R. Dronskowski, *J. Phys. Chem. A*, 2011, **115**, 5461–5466.
- [15] S. Maintz, V. L. Deringer, A. L. Tchougréeff and R. Dronskowski, *Journal of Computational Chemistry*, 2013, **34**, 2557–2567.
- [16] S. Maintz, V. L. Deringer, A. L. Tchougréeff and R. Dronskowski, *J. Comput. Chem.*, 2016, **37**, 1030–1035.